FULL PAPER

ADVANCED
FUNCTIONAL
MATERIALS

Transsision-Metal-Dichalcogenide

www.afm-journal.de

Humidity-Controlled Ultralow Power Layer-by-Layer Thinning, Nanopatterning and Bandgap Engineering of MoTe$_2$

V. Karthik Nagareddy, Toby J. Octon, Nicola J. Townsend, Saverio Russo, Monica F. Craciun, and C. David Wright*

A highly effective laser thinning method is demonstrated to accurately control the thickness of MoTe$_2$ layers. By utilizing the humidity present in the ambient atmosphere, multilayered MoTe$_2$ films can be uniformly thinned all the way down to monolayer with layer-by-layer precision using an ultralow laser power density of 0.2 mW µm^{-2}. Localized bandgap engineering is also performed in MoTe$_2$, by creating regions with different bandgaps on the same film, enabling the formation of lateral homojunctions with sub-200 nm spatial resolution. Field-effect transistors fabricated from these thinned layers exhibit significantly improved electrical properties with an order of magnitude increase in on/off current ratios, along with enhancements in on-current and field-effect mobility values. Thinned devices also exhibit the fastest photoresponse (45 µs) for an MoTe$_2$-based visible photodetector reported to date, along with a high photoresponsivity. A highly sensitive monolayer MoTe$_2$ photodetector is also reported. These results demonstrate the efficiency of the presented thinning approach in producing high-quality MoTe$_2$ films for electronic and optoelectronic applications.

1. Introduction

Among the family of semiconducting transition metal dichalcogenides (TMDCs), molybdenum ditelluride (MoTe$_2$) is one of the most intriguing but relatively less explored materials.[1,2] Bulk 2H-MoTe$_2$ is an indirect bandgap semiconductor with an optical gap of around 0.8 eV,[3] while the monolayer and bilayer possess a direct bandgap, similar to that of Si ($\approx$1.1 eV), thus

Dr. V. K. Nagareddy, T. J. Octon, N. J. Townsend, Prof. S. Russo,
Prof. M. F. Craciun, Prof. C. D. Wright
Centre for Graphene Science
College of Engineering
Mathematics and Physical Sciences, Harrison Building
North Park Road
University of Exeter
Exeter EX4 4QF, UK
E-mail: david.wright@exeter.ac.uk

The ORCID identification number(s) for the author(s) of this article can be found under https://doi.org/10.1002/adfm.201804434.

extending the spectral range of semiconducting TMDCs from visible to the near-IR region.[1,4] The electrical and optical properties of 2H-MoTe$_2$ have been exploited for a range of applications, including ambipolar field-effect transistors (FETs),[5] complementary metal–oxide–semiconductor (CMOS) based inverters and amplifiers,[5,6] light-emitting diodes,[7] ultrafast photodetectors,[8] and highly sensitive gas sensors.[9] However, the advancement of these applications for practical purposes has been severely hindered by the less mature film synthesis process for MoTe$_2$ compared to that of other widely studied TMDCs such as MoS$_2$, MoSe$_2$, WS$_2$, and WSe$_2$. While the large area growth of 2H-MoTe$_2$ films of various thicknesses has been demonstrated by a wide range of techniques, including chemical vapor deposition (CVD),[10,11] physical vapor deposition (PVD),[12] metal-organic CVD (MOCVD),[13] and molecular beam epitaxy (MBE),[14] the growth of films with precisely controlled (i.e., user-defined) thicknesses, right down to monolayer, remains elusive. This is mainly due to the small electronegativity difference (0.3 eV) between Mo and Te atoms, which leads to low chemical reactivity and significantly weaker bonding energy of Mo—Te bonds, making it very challenging to obtain atomically thin stoichiometric 2H-MoTe$_2$ films.[11] As a result, the production of ultrathin 2H-MoTe$_2$ layers has been primarily limited to mechanical exfoliation, which lacks precise control over the resulting film thickness.

To provide better control of the thickness of TMDC films, several top-down techniques have been developed, including chemical,[15] thermal,[16] plasma,[17] and laser treatments.[18] The laser-thinning approach offers several attractions, being inherently simple, low cost and, importantly, can be used to selectively pattern films and devices at sub-micrometer scale resolution without the need for complicated lithographic processing. Nevertheless, to date this approach has lacked precise control over the final film thickness (due to the heat transfer and dissipation mechanism of the high power continuous wave (CW) lasers that have been used in the majority of laser-thinning studies reported previously).[18–21] For example, Castellanos-Gomez et al.,[18] reported thinning MoS$_2$ samples to monolayers from bulk material with an initial thickness of around 20 layers, but without any control over layer precision during thinning. Hu et al.,[21] did show some thickness control in MoS$_2$, but were

limited to producing thicknesses of three layers or below and needed multiple laser scans to achieve this control. Importantly, the laser exposure times and power densities required for thinning TMDCs reported so far are rather high, being in the range of 100–600 ms and 30–80 mW μm^{-2}, respectively.[18–21] In addition, laser thinning was also previously found to increase the surface roughness of TMDCs by around 3–4 times, affecting the crystal quality and thus the overall electrical properties of thinned samples.[18,22] Thus, despite its huge potential, using a laser-thinning route to producing thickness-controlled TMDC layers with no physical modification to the thinned layers has so far proved extremely challenging.

Herein, we demonstrate a novel and highly effective humidity-controlled thinning approach to accurately define the thickness of $MoTe_2$ layers using CW laser irradiation. For the first time we show that by utilizing humidity present in the ambient atmosphere, we can achieve layer-by-layer thickens control, irrespective of the initial sample thickness. In particular, we could achieve this thickness control using much faster laser exposure times (1 ms) and far lower laser powers (0.2–4 mW μm^{-2}) than previously imagined possible. Our approach also leads to excellent surface quality of thinned samples, without any topographical or structural damage to the $MoTe_2$ crystal lattice. In addition, we carry out localized bandgap engineering by creating regions with different bandgaps on the same sample, enabling the formation

of lateral homojunctions with sub-200 nm spatial resolution. The thickness changes were examined by optical microscopy, atomic force microscopy (AFM), Raman and photoluminescence (PL) spectroscopy. The electrical and optical properties of selectively laser-thinned $MoTe_2$ were also investigated by fabricating FETs, which showed significantly superior device performance compared to their pristine counterparts.

2. Results and Discussion

Multilayered $MoTe_2$ flakes were mechanically exfoliated from a bulk 2H-$MoTe_2$ crystal (*hq-graphene Inc.*) and transferred on to Si/SiO_2 (300 nm) substrates by the standard exfoliation process.[23] Laser thinning was then performed using a confocal Raman spectrometer coupled to an AFM, which is enclosed in a humidity controlled environmental chamber, as shown in **Figure 1**a. This Raman/AFM setup allows us to acquire in situ Raman spectra, surface topography and optical contrast of $MoTe_2$ films before and after thinning.

First, we investigated the laser power threshold of $MoTe_2$ by exposing several samples of similar thicknesses (≈3.7 nm) to a focused laser beam (λ = 532 nm) with excitation powers ranging from 0.02 to 30 mW μm^{-2}. Here the samples were placed on a motorized AFM stage and raster scanned at an optimized laser exposure time and scan step-size of 1 ms and
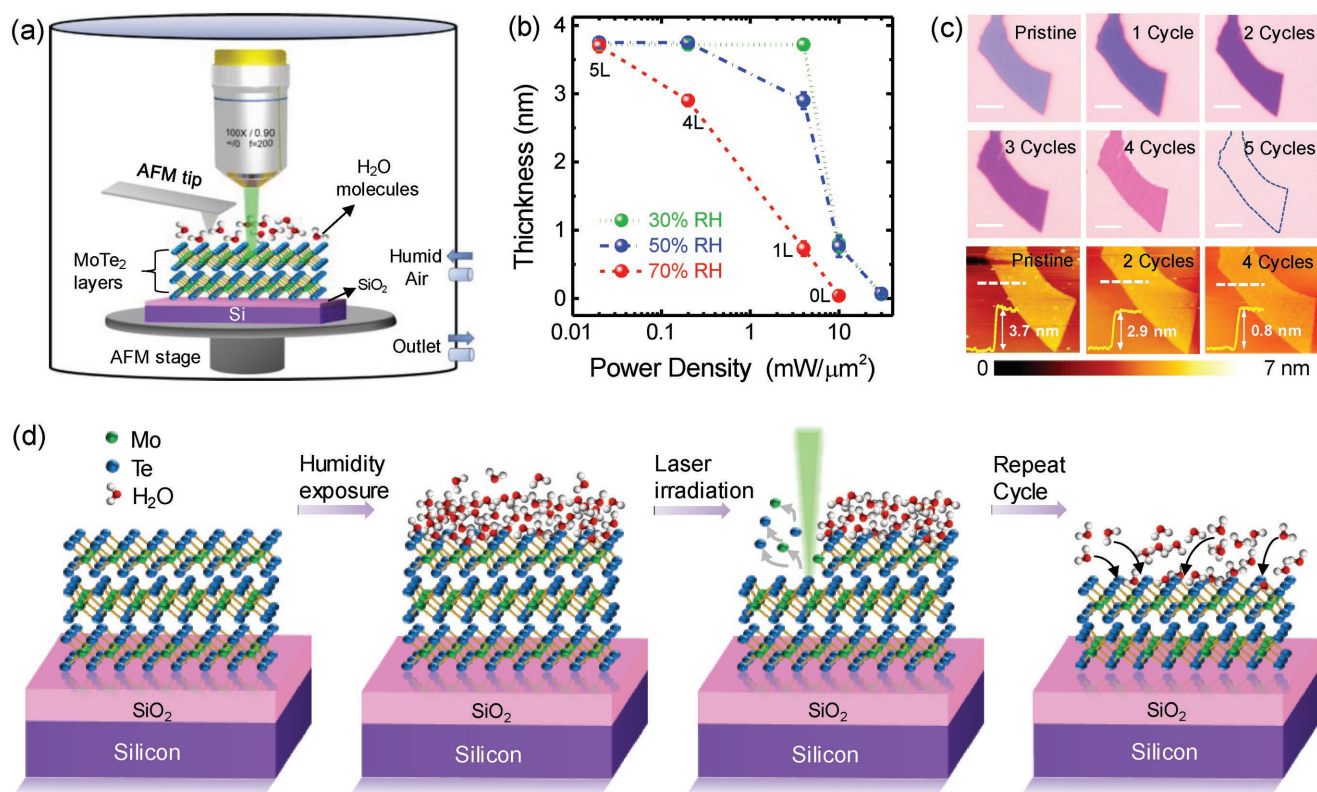

Figure 1. a) Schematic illustration of the experimental setup used for thinning and in situ imaging of $MoTe_2$. b) Change in thickness of multilayered $MoTe_2$ samples as a function of incident laser power at different humidity levels. c) Optical microscope images (top 2 panels) and corresponding AFM topography images (bottom panel) of $MoTe_2$ samples after each thinning cycle. d) Schematic illustrations explaining the suggested $MoTe_2$ photochemical thinning mechanism.

1804434 (2 of 9)

200 nm, respectively. This dose test experiment was performed in the ambient atmosphere at three different humidity levels; low-level (20–40% relative humidity (RH)), intermediate-level (40–60% RH) and high-level (60–80% RH), to analyze the influence of water vapor on the thinning process.

The plot in Figure 1b shows the change in $MoTe_2$ film thickness as a function of laser power for all three humidity levels. Under low water vapor concentrations (≈30% RH), the thickness of pristine $MoTe_2$, which was confirmed through AFM measurements as 3.77 nm (5L), remains unaffected for laser powers up to 4 mW μm^{-2}, but uncontrollably (i.e., suddenly) thinned down to 0.9 nm (1L) when the power was increased to 10 mW μm^{-2}. At intermediate humidity levels (≈50% RH), some thickness control was achieved for (relatively low) laser powers ≥ 4 mW μm^{-2}. Nevertheless, the most intriguing behavior was observed at the highest humidity level (≈70% RH), where a multilayer film of 3.7 nm (5L) was controllably thinned to 2.9 nm (4L) at an exceptionally low excitation power of 0.2 mW μm^{-2}. Moreover, subsequent laser scans with the same incident power led to continuous thinning of the flake from 2.9 nm (4L) to 2.2 nm (3L) and to 1.5 nm (2L) for thinning cycles of 1, 2, and 3, respectively. Figure 1c shows optical microscope and AFM images of these layer-by-layer thinned samples, exhibiting a clear change in optical contrast, corresponding to the change in thickness after each cycle. To further reduce the thickness from 2L to 1L, a slightly higher power of 4 mW μm^{-2} was needed to overcome the heatsink effect from the substrate. On increasing the laser power further to 10 mW μm^{-2}, total ablation of the $MoTe_2$ occurred, as evident from the disappearance of optical contrast (Figure 1c, 5-cycle case) and further confirmed by Raman and PL measurements (see below). These results show that it is possible to engineer the thickness of, or even completely etch away, $MoTe_2$ layers at ≤ 10 mW μm^{-2} laser power. Interestingly, such power densities are routinely used in Raman and PL characterization of many TMDCs, including $MoTe_2$.[4,24] Although brief exposure to such low power densities does not adversely affect the film quality,[25] our results clearly demonstrate that when operated in a high humidity environment, unintended etching (thinning) or damage to the film could indeed occur even for very short exposure times (<1s). Therefore, as well as offering a new route to user-defined control of TMDC film thickness, our work shows that due care must be taken while performing optical characterization of TMDCs, particularly $MoTe_2$ in ambient atmosphere, so to avoid inadvertent, unplanned thinning.

The AFM measurements in Figure 1c (bottom panel) reveal uniform laser-thinning of $MoTe_2$. Remarkably, the surface morphology of all thinned samples improved considerably, in which the average root-mean-square (RMS) roughness was reduced from ≈0.7 nm (pristine) to ≈0.2 nm (thinned), indicating excellent surface quality of thinned layers (this reduced roughness is mainly attributed to the removal of residues present on the topmost layer as a result of mechanical exfoliation; see Figure S3, Supporting Information). This is significant because, unlike other thinning techniques which show increased surface roughness after thinning,[13,18,22] the thinning approach employed here produces atomically smooth surfaces, highlighting the nondestructive nature of the process. Our system can also achieve fast scanning rates of up to 10 $\mu m\ s^{-1}$, thus enabling rapid thinning and imaging of large area multilayer $MoTe_2$ films, such as those grown by recently developed vapor-phase methods.[10,11] Schematic illustrations in Figure 1d depict the layer-by-layer thinning mechanism of $MoTe_2$ by our proposed photochemical process (see later).

The structural and optical properties of the thinned films were evaluated by Raman and PL spectroscopies respectively, using <0.05 mW μm^{-2} excitation power at 30% RH to avoid unintentional thinning/etching. **Figure 2**a shows the evolution of Raman spectra after each thinning cycle, exhibiting characteristic peaks at ≈170 cm^{-1} (A_{1g}), ≈235 cm^{-1} (E^1_{2g}), and ≈289 cm^{-1} (B^1_{2g}), corresponding to phonon modes of 2H-$MoTe_2$ crystal,[26] along with a reference Si-peak at 520 cm^{-1}. The intensity of these peaks varied significantly after each thinning cycle, in which the Si-peak increased and the E^1_{2g} peak decreased with the decreasing layer thickness, due to the reduced optical absorption of thinner $MoTe_2$ layers. The ratio of these peaks (E^1_{2g}/Si) displayed a linear increment with the increasing layer number (Figure 2b), thus permitting accurate identification of $MoTe_2$ film thickness.[26] Note that, apart from the peaks related to $MoTe_2$ and Si, no other peaks associated with oxidized $MoTe_2$ (i.e., MoO_3, MoO_2, and TeO_2) were observed in the Raman spectra of all thinned samples, indicating that the $MoTe_2$ surface is not affected by oxidation during the thinning process (see Figure S4, Supporting Information). Additionally, the PL and electrical measurements (detailed below) support that the thinned $MoTe_2$ layers exhibit semiconducting and not insulating behavior (the latter being expected for oxidized $MoTe_2$).

The crystalline quality of our controllably thinned $MoTe_2$ films was determined by analyzing the Raman peak line widths. Since the full width at half-maximum (FWHM) of a Raman peak is commonly used to gauge the crystal quality of a material, with narrower peaks corresponding to higher crystallinity and vice-versa, any changes to the $MoTe_2$ lattice would readily reflect upon the Raman peak width.[27] The FWHM of thinned layers showed negligible change (i.e., broadening), when compared to their pristine counterparts (Figure 2b), indicating that the structural integrity of the film is fully preserved following the thinning process. This was further confirmed by the strong correlation observed between the PL peak line widths of thinned and pristine $MoTe_2$ layers, shown in Figure 2e.

Figure 2c shows the emergence of PL spectra of $MoTe_2$ layers, in which the pristine 5L, as well as thinned 4L and 3L films, exhibit weak PL features at ≈1.03 eV, implying indirect optical transitions dominate few-layer $MoTe_2$.[4,28] However, after reducing the film thickness to 2L and 1L, the exciton peak energy blue shifts to ≈1.04 and ≈1.07 eV, respectively, while the associated PL intensities dramatically increase, suggesting that direct optical gap transitions dominate thinned monolayer and bilayer $MoTe_2$, in agreement with previous studies.[4,28] A small redshift in the peak energy (3–7 meV) was observed for all laser-thinned samples with respect to the pristine layers (Figure 2d,e), which is attributed to doping by adsorbed H_2O and O_2 molecules during the thinning process (see the Supporting Information).

To demonstrate the precision of our thinning technique, experiments were performed on an $MoTe_2$ sample consisting of different thicknesses, ranging from two layers to
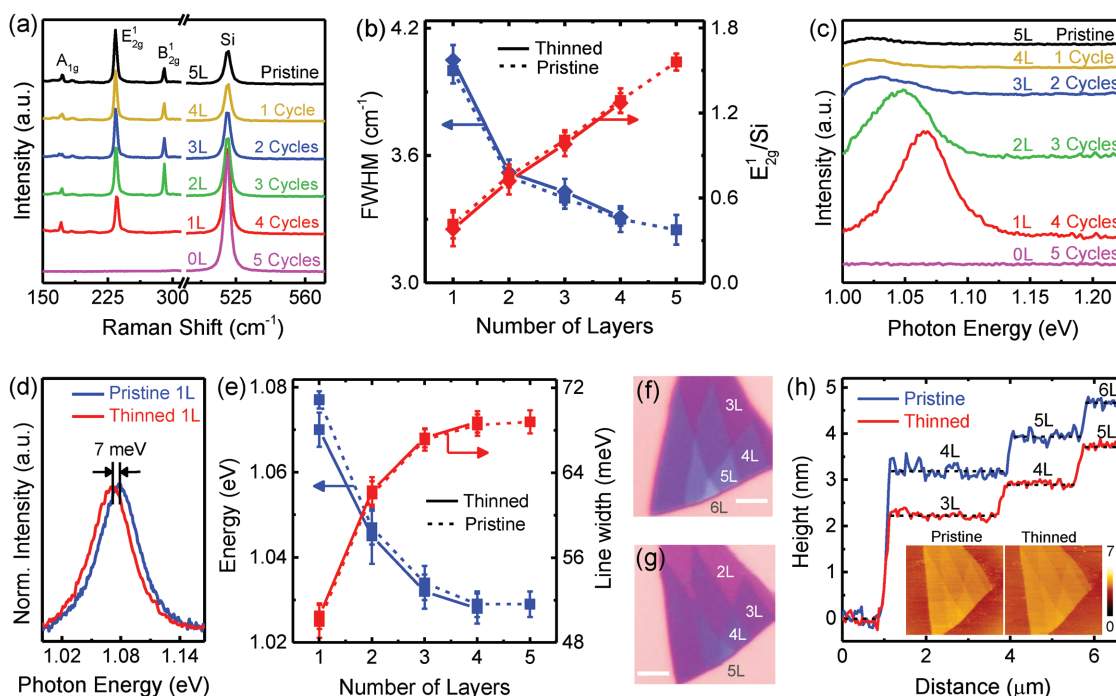
**ADVANCED
SCIENCE NEWS**
www.advancedsciencenews.com

**ADVANCED
FUNCTIONAL
MATERIALS**
www.afm-journal.de

Figure 2. a) Evolution of Raman spectra of MoTe$_2$ after each thinning cycle. b) FWHM and peak intensity ratios of thinned and pristine MoTe$_2$ as a function of number of layers. c) PL spectra of MoTe$_2$ recorded after each thinning cycle. d) Comparison of the pristine and thinned monolayer MoTe$_2$ PL spectra. e) Change in PL peak energy and line width of pristine and thinned MoTe$_2$ as a function of number of layers. Optical microscope images of a sample consisting of different thickness f) before and g) after one thinning cycle. h) AFM topography (inset) of the sample in (f) and (g) and their corresponding height profile scans.

six layers, as shown in Figure 2f. After one laser scanning cycle (at 0.2 mW μm^{-2} and 70% RH), the local thickness variations within the flake can still be seen, albeit with different optical contrasts as compared to that of the pristine sample (Figure 2g). The AFM measurements in Figure 2h confirmed that a single monolayer has been removed at the respective regions of the sample, with each area of the sample reducing by the same amount, revealing the isotropic etching rates of our thinning process.

In order to understand in more detail, the effect of humidity on our layer-by-layer thinning process, cyclical thinning experiments were performed on a freshly exfoliated MoTe$_2$ film of ≈6.7 nm (nine layers) thickness, using a fixed laser power of 0.2 mW μm^{-2} under different RH levels, ranging from 30% to 90%. Under low humidity conditions (< 60% RH), no detectable change in thickness was observed even after three laser scanning cycles, as shown in **Figure 3**a. However, on repeating the scan at a high humidity level (70%), with all other parameters remaining constant, an immediate change in thickness was observed for the scanned region, as evident from the AFM topography in Figure 3a inset (top right). The line profile scan (Figure S5, Supporting Information) confirmed that a monolayer was locally removed from the scanned region (3 μm × 3 μm), without affecting the thickness of the surrounding areas.

Successive scanning in the same region resulted in continuous thinning of the sample, provided the humidity level is above 65%. For example, after performing two successful etch cycles under high humidity (>65%), the chamber was returned to intermediate humidity levels (around 40–60% RH), followed

by another round of laser scanning cycles with the same incident power of 0.2 mW μm^{-2}. Under these low humidity conditions, no apparent change in thickness was seen, consistent with the above observations. However, increasing the humidity again to 70% RH, thinning resumed under laser irradiation, illustrating the critical role of water molecules on the thinning process.

Figure 3b shows AFM topography images (inset) and corresponding height profiles obtained for different thinning cycles. Figure 3c plots the resultant etch depth as a function of the number of thinning cycles, along with the measured surface roughness (inset). A linear increase in etch depth was obtained with increasing number of thinning cycles (at 70% RH), with a slope of ≈0.76 nm, indicating the removal of one monolayer per thinning cycle. This demonstrates that by controlling the humidity in the surrounding environment, layer-by-layer thinning of MoTe$_2$ can be realized at ultralower power densities using CW lasers.

We have also performed localized bandgap engineering in MoTe$_2$ to create lateral homojunctions with different bandgaps on the same sample. Figure 3d (top panel) shows the optical image of a pristine MoTe$_2$ sample of predominantly 3L thickness that was deterministically thinned by irradiating selected regions with laser powers ranging from 0.2 to 30 mW μm^{-2} at 70% RH. By moving the scanning stage in a programmed fashion during laser exposure, a continuous sequence of a 3L, 2L, 1L, and 0L pattern is fabricated, as shown in Figure 3d (middle panel). This patterned sample was scanned again (at a reduced power of 0.02 mW μm^{-2} and at 30% RH, where no thermal or etching effects occur) to obtain the Raman
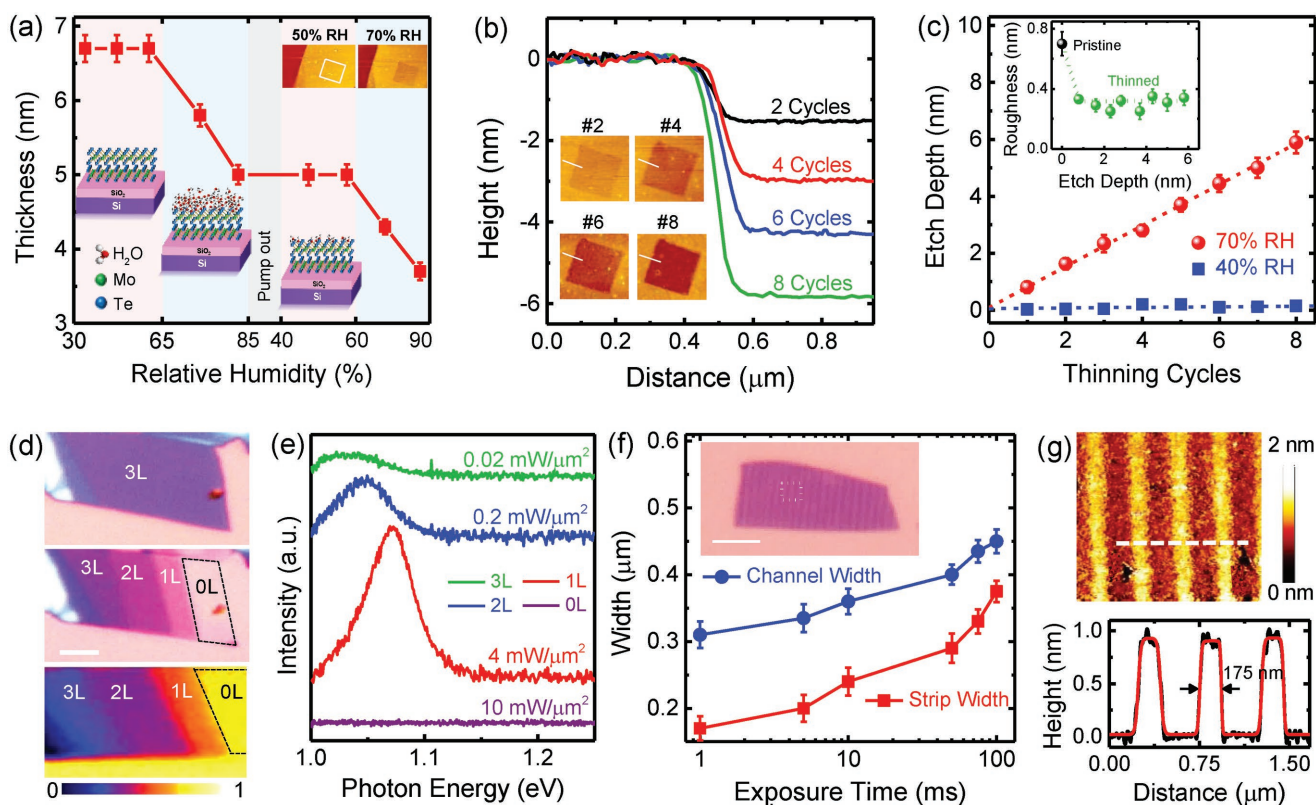
Figure 3. a) Change in thickness of a multilayered $MoTe_2$ sample as a function of varying RH levels under constant laser exposure of 0.2 mW μm^{-2}. The top inset shows AFM topography images of the sample taken after undergoing laser scanning cycles at 50% RH (left) and 70% RH (right). The bottom inset shows a schematic of the process at various humidity levels. b) AFM topography (inset) and height profile scans of a repeatedly scanned $MoTe_2$ flake, resulting in progressively deeper etching. c) Plot showing the $MoTe_2$ etch depth as a function of number of thinning cycles at high (70%) and intermediate (40%) humidity levels (inset shows surface roughness vs etch depth). d) Optical microscope images of a pristine 3L sample (top), deterministically patterned into 3L/2L/1L homostructures (middle) and the resultant Raman intensity map (bottom). e) PL spectra of $MoTe_2$ taken from the 3L/2L/1L/0L regions. f) Width of nanochannels and nanostrips as a function of laser exposure time. Inset shows optical image of the patterned bilayer sample (scale bar 3 μm). g) AFM topography image of the patterned $MoTe_2$ nanostrips and nanochannels and the corresponding height profile. The red solid line is the fitting for the height profile scan.

intensity map of the Si-peak (Figure 3d, bottom panel). Since the intensity of this Si-peak is proportional to the thickness of $MoTe_2$ atop the substrate, any change in $MoTe_2$ thickness can be unambiguously determined. A gradual increment in Si-peak intensity was observed along the patterned regions of the sample starting from the pristine 3L region through to the 0L region, corresponding to the reducing $MoTe_2$ thickness. The homogeneous intensity distribution over the surfaces of each thinned layer demonstrates spatially uniform thinning and removal of $MoTe_2$. The PL spectra acquired from these thinned regions exhibited strong enhancements in peak intensity at ≈1.06 eV and ≈1.08 eV (Figure 3e), representing 2L and 1L $MoTe_2$, respectively, while no signal was detected from the "0L" region, confirming the successful thinning and ultimately removal of $MoTe_2$.

Figure 3f shows some of the nanopatterning capabilities and resolution of our thinning process. Here we systematically varied the laser exposure time from 1 to 100 ms (fixing the laser power to 4 mW μm^{-2}) and measured the width of the resulting thinned channel and (unthinned) strip separating the channels. As can be seen in Figure 3f, for the shortest exposure time of 1 ms (only limited here by our experimental set-up),

we achieved the smallest strip and channel widths of 170 and 300 nm, respectively. By increasing the spacing between channels and tuning the laser exposure times simultaneously, different strip and channel widths were realized, as also shown in the Figure 3f. Note that the inset of Figure 3f shows the optical image of a bilayer film patterned into a series of channels and strips using 1 ms laser exposure. The corresponding AFM topography in Figure 3g shows the fabricated nanopatterns, exhibiting a clear distinction between thinned monolayer channels (dark regions) and the resultant bilayer strips (bright regions), leading to a seamless integration of a monolayer channel and bilayer strip architecture. The height profile scan reveals that strip and channel widths as narrow as 170 and 300 nm, respectively, can be fabricated with this technique, demonstrating its capability for on-demand fabrication of user-defined structures in $MoTe_2$ crystals under standard atmospheric conditions (and controlled humidity) with high spatial resolution and extremely fast process times.

We note that laser induced etching/thinning has been demonstrated previously for a wide range of materials, including TMDCs, where the principle etching mechanism is either due to photothermal or photochemical processes. The photothermal

mechanism is dominant at high laser powers, where the energy transfer from the laser leads to a rapid rise in local temperatures, resulting in fast vaporization/sublimation of the material. Such a thermal driven thinning process, employing high intensity laser irradiation has been reported in the literature for several 2D materials, including MoTe$_2$.[18,19,22,29] However, this approach produces uncontrolled reduction in sample thickness and usually exhibits excessive surface roughness after thinning. Moreover, from Raman peak analysis (Figure S8, Supporting Information), the maximum rise in local temperature during our thinning process is estimated to be only ≈90 K. Since the sublimation temperature of Te is > 650 K (375 °C),[19,29] the temperatures generated during our laser thinning process are incapable of causing any thermal induced structural damage to MoTe$_2$, suggesting that the decomposition of MoTe$_2$ in our work is predominantly photochemical and not photothermal.

Photochemical etching, on the other hand, does not require high laser powers and can be achieved by employing low intensity lasers with a photon energy greater than the bandgap of the target material. In this case, the photon absorption generates electron–hole pairs in the material, which leads to bond dissociation in the presence of reactant species, resulting in decomposition of the material with minimal thermal effects. Although the photochemical etching mechanism has been widely studied in conventional semiconductors such as Si, GaAs, AlGaAs, etc.,[30,31] its usefulness in 2D materials has only been recently demonstrated by Bobrinetskiy et al.,[32] via the etching and patterning of graphene layers. In that study, using residual water molecules as reactant species, graphene was successfully etched at laser powers below the ablation threshold by introducing defects and creating vacancies in the graphene sheet. Moreover, the authors explained the photochemical etching of graphene as being initiated by the generation of electron/hole pairs, which take part in redox reaction between graphene and water molecules, generating $sp3$ defects and vacancies in the graphene lattice, hence graphene etching.

Adopting a similar model as Bobrinetskiy et al.,[32] we suggest that the thinning mechanism of MoTe$_2$ in our case is photochemical, as follows. At high water vapor concentrations (>65% RH), H$_2$O molecules are expected to occupy all available adsorption sites on MoTe$_2$, resulting in a thin continuous water layer forming on the MoTe$_2$ surface. When a focused laser beam (λ = 2.33 eV/532 nm) is irradiated on to this water adsorbed MoTe$_2$ (E_g = ≈1 eV), nonlinear absorption of photons takes place,[33] leading to highly excited free electron generation in MoTe$_2$ (MoTe$_2$ + $h\upsilon$ → MoTe$_2$*), whose steady-state population depends on the photon flux, absorption cross-section and recombination rate. These photoexcited charge carriers participate in the chemical reaction with the adsorbed water molecules on the MoTe$_2$ surface, effectively hole doping MoTe$_2$ and generating hydroxyl (−OH) radicals which in turn react with MoTe$_2$, triggering the photochemical activity and breaking of Mo−Te bonds.[34] As the MoTe$_2$ films (both exfoliated and grown) always contain stable defects such as Te vacancies in the lattice, it is likely that the photochemical etching is initiated at these defect sites, due to the loosely bound Mo and Te atoms, and expands laterally toward the basal planes.

In general, materials with high absorption coefficients and low thermal conductivities display better photochemical etching efficiency rates,[30] since the transfer of laser energy to electron excitation is more efficient. Among the semiconducting TMDCs, MoTe$_2$ has highest absorption coefficient (≈3 × 10^6 cm^{-1})[35,36] and lowest thermal conductivity (≈20 W m^{-1} K^{-1}),[37,38] while the bond energy of Mo−Te is also significantly weaker than other TMDCs, due to the small electronegativity difference between Mo and Te atoms (≈0.3 eV). As a result, the dissociation and photochemical decomposition of MoTe$_2$ is expected to occur with very modest rise in surface temperatures, as we have observed here.

Since the photochemical reactions take place only at the irradiated regions of the sample covered with H$_2$O molecules, the thinning of MoTe$_2$ proceeds sequentially. For example, as the adsorption of water molecules will be mainly concentrated on the surface of MoTe$_2$ (i.e., at the topmost layer, which shields the remaining layers underneath), etching is mainly expected to proceed along this water adsorbed top layer and self-terminates as soon as it reaches the next layer due to the unavailability of enough water molecules for the photochemical reaction to take place. However, after completely removing the top layer, water molecules readsorb on to the freshly exposed MoTe$_2$ layer and the photochemical etching resumes upon laser irradiation. This process can be repeated layer-by-layer until the desired thickness is obtained (see Figure 1d), thus providing great control in fabricating MoTe$_2$ sheets with user-defined thickness.

Finally, we point out that the electrical performance of MoTe$_2$ films fabricated using our photochemical thinning process is excellent, exceeding that of pristine exfoliated flakes (at least in the FET configuration examined here). **Figure 4**a shows a schematic illustration of photochemical thinning of an MoTe$_2$ FET. The electrical properties of pristine (14L) and laser-thinned (9L) devices are shown in Figure 4b, exhibiting p-type behavior, as reported by others for few- and multilayer MoTe$_2$.[2,39] The gate voltage position of the current minimum (V_{min}) of the thinned device significantly shifted from −3 V (pristine) to +48 V (thinned), indicating strong p-type doping after photochemical treatment. The thinned devices showed minor changes in hole mobility from 12.4 to 13.5 cm^2 V^{-1} s^{-1}, while the current on/off ratio increased by an order of magnitude from 2 × 10^3 to 3 × 10^4 due to an enhancement of the on-state current and a substantial reduction in off-state current. In order to verify if the improved electrical characteristics observed here are indeed due to laser thinning process and not due to the redcution in MoTe$_2$ thickness, we also fabricated a pristine 9L device and directly compared its electrical characteristics with that of a thinned 9L device. As can be seen in Figure S12 (Supporting Information), the thinned device exhibited ehnanced on-current, and noticeable improvement in field-effect mobility from 6.4 cm^2 V^{-1} s^{-1} (pristine device) to 13.5 cm^2 V^{-1} s^{-1} (thinned device), demonstrating the role of our laser thinning process in enhancing the overall performance of TMDC devices.

Similar performance improvements were observed for several other thinned devices when compared to pristine MoTe$_2$ channels. For example, Figure 4c shows the transfer characteristics of an MoTe$_2$ device that was thinned from ≈3 nm (4L) to ≈0.8 nm (1L) using 4 mW μm^{-2} power. The hole mobility of the pristine 4L device was calculated as 0.2 cm^2 V^{-1} s^{-1}, which is

ADVANCED
SCIENCE NEWS
www.advancedsciencenews.com

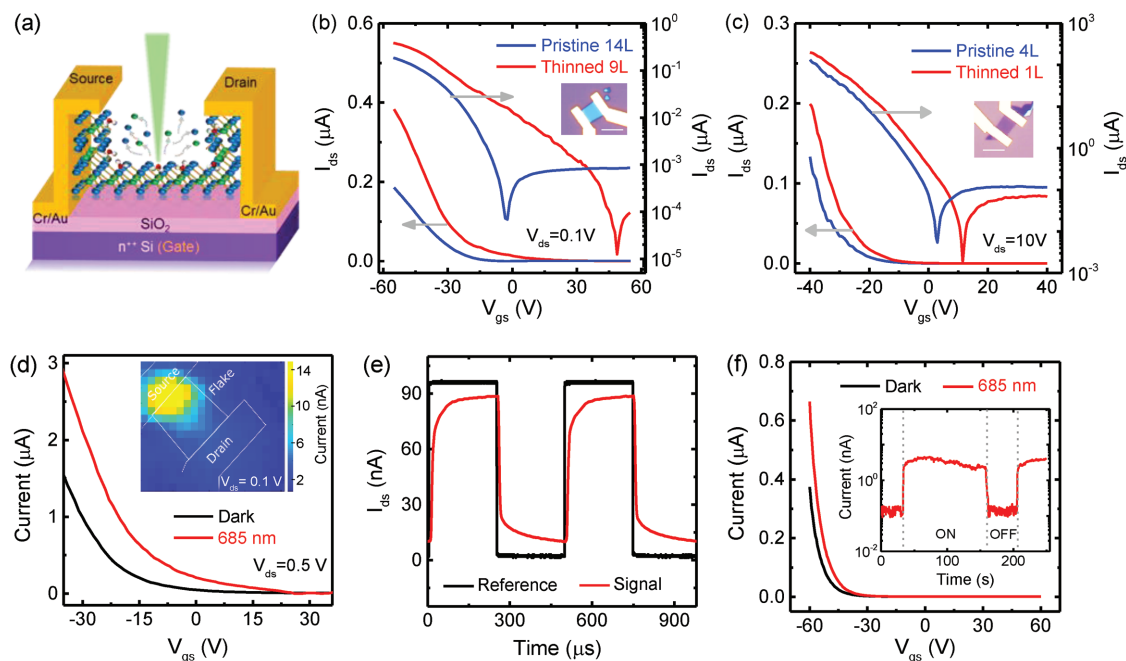ADVANCED
FUNCTIONAL
MATERIALS
www.afm-journal.de

Figure 4. a) Schematic illustration of photochemical thinning of an MoTe$_2$ FET. I_{ds}–V_{gs} transfer characteristics of b) a pristine 14L and thinned 9L MoTe$_2$ device and c) a pristine 4L and thinned 1L MoTe$_2$ device, plotted in linear and logarithmic scales. The insets in (b) and (c) show the optical microscope images of thinned 9L and thinned 1L devices. Scale bar is 3 µm. d) I_{ds}–V_{gs} characteristics of the thinned 9L device under dark and laser illumination (λ = 685 nm, 6 µW power). Inset shows the photocurrent map of the device. e) Time-resolved photoresponse of thinned multilayer (9L) MoTe$_2$ device excited with 685 nm laser and 6 µW power. f) I_{ds}–V_{gs} characteristics of a thinned monolayer device in dark and laser illumination conditions (λ = 685 nm, 3 µW power). Inset shows the temporal photoresponse of the device for laser on/off cycles.

consistent with other studies of similar thickness and without applying any intentional doping or dielectric engineering techniques.[5,8,40] After thinning it to 1L, a small increase in mobility to ≈0.3 cm^2 V^{-1} s^{-1} was observed, saturating at ≈1.0 cm^2 V^{-1} s^{-1} (for V_{ds} = 4V), which is in fact the highest mobility value reported to date for a monolayer MoTe$_2$ FET (see Figure S11, Supporting Information). Similar to the multilayer case, the on/off ratio of this thinned monolayer device increased by an order of magnitude from 2×10^4 to 1×10^5. This value is significantly better than commonly achieved values for uncapped MoTe$_2$ devices measured in the ambient atmosphere;[41,42] indeed, it is very close to the best reported on/off ratios in the literature for a monolayer MoTe$_2$ FET that was encapsulated between h-BN layers[6] (see Figure S11, Supporting Information). It is also worthwhile noting that the thinned devices showed very good resistance to atmospheric oxidation/degradation, with the device of Figure 4c for example, showing excellent electrical and optical properties even after 10 days of ambient exposure.

To further illustrate the improved functionality of photochemically thinned films/devices, photoelectrical measurements were performed on MoTe$_2$ photodetectors. Figure 4d inset shows the photocurrent map, acquired by scanning the focused laser beam (λ = 685 nm, 6 µW) across a thinned multilayer (9L) device, which reveals that the photocurrent generation primarily occurs at the metal-MoTe$_2$ interface, as reported previously.[8] Figure 4d shows electrical characteristics of the thinned multilayer (9L) device under dark and laser illumination conditions (λ = 685 nm), where the incident power was fixed at 3.5 µW µm^{-2}, much lower than that used for thinning

experiments. Under illumination, a clear increase in device current was observed with increasing negative gate voltages (ON-state region), exhibiting a strong photogating effect.[8] The maximum photoresponsivity (R) of the multilayer device (defined as the ratio of the photocurrent, I_{pc} and the incident laser power, P_{inc}) was measured to be 0.24 A W^{-1} for a laser power of 6 µW (see also Supporting Information (Section S11)), which can be further increased significantly by using lower laser powers, as demonstrated in our previous work.[8] Figure 4e presents the time-resolved photoresponse of the thinned multilayer device for different laser on/off cycles, from which we can determine the rise and fall time of the photocurrent (defined here as the time taken for the device to go from 10% to 90% of the total photocurrent and vice-versa). The rise and fall times were measured as 45 µs and 35 µs, respectively, which are the fastest photoresponse times reported for MoTe$_2$-based *visible* light photodetectors to-date,[8,43–46] demonstrating the significant advantage of our photochemical thinning method in fabricating high-quality functional electronic and optoelectronic devices (see Figures S10–S18, Supporting Information for additional device results).

In addition to the thinned multilayer device, we also show for the first time the photoresponse behavior of a monolayer MoTe$_2$ device, see Figure 4f. The device current significantly increased under laser illumination in the ON-state region, as expected, exhibiting a maximum photoresponsivity of 0.1 A W^{-1}, which is considerably higher than the commonly achieved photoresponsivity values for devices with thick MoTe$_2$ channels. This high photoresponsivity is attributed to the direct

bandgap of monolayer $MoTe_2$, which allows higher absorption coefficient and efficient electron–hole pair generation under photoexcitation.

3. Conclusion

In summary, we have demonstrated a simple yet highly effective, user-controllable, thinning process for $MoTe_2$ using CW laser irradiation. By utilizing the humidity present in the ambient atmosphere, we have achieved layer-by-layer thinning precision in multilayered $MoTe_2$ at an ultralow laser power density of 0.2 mW μm^{-2}, without affecting the crystal quality. Localized bandgap engineering in $MoTe_2$ was also achieved, by creating regions with different bandgaps on the same sample, enabling the formation of lateral homostructures with sub-200 nm spatial resolution. The thinning process is highly selective in which only the top layer, having a high concentration of adsorbed water molecules, participates in a photochemical etching reaction. Unlike other laser thinning studies, which are predominantly based on photothermal thinning, i.e., thermal sublimation of chalcogen atoms due to local rise in temperatures of >670 K, our approach follows photochemical thinning behavior, where only a moderate rise in temperatures of ≈100 K was observed due to extremely low laser powers involved. Such low irradiation temperatures are likely to prove useful when directly thinning TMDC samples on temperature sensitive substrates such polydimethylsiloxane (PDMS), polyethylene terephthalate (PET), polyethylene naphthalate (PEN), etc., which are commonly used in flexible electronics applications.

The electrical characteristics of photochemically thinned $MoTe_2$ FETs showed an order of magnitude increase in on/off current ratios, along with improved on-current and field-effect mobility values. The photoelectrical properties of a photochemically thinned multilayer device exhibited the fastest photoresponse (45 μs) for a $MoTe_2$-based visible photodetector reported to date, along with high photoresponsivity. We have also reported for the first time, a highly sensitive monolayer $MoTe_2$ photodetector. These results demonstrate the efficiency of our photochemical thinning method in producing high quality $MoTe_2$ films for electronic and optoelectronic applications. The generality of this technique suggests that it can be widely applied to other TMDCs to produce high quality, geometrically well-defined and nanopatterned films for both fundamental studies and for future device prototyping.

4. Experimental Section

Sample Preparation: Few-layer and multilayer $MoTe_2$ flakes were obtained by mechanical exfoliation from a bulk 2H-$MoTe_2$ crystal purchased from *HQ graphene Inc.* and transferred on to Si/SiO$_2$ (300 nm) substrates using adhesive tape and PDMS stamp technique described previously.[23] All exfoliated flakes were thoroughly cleaned in warm acetone (≈45 °C) to remove polymeric residues from $MoTe_2$ surfaces, followed by a quick rinse in isopropyl alcohol and deionized water.

AFM and Raman Characterization: AFM and Raman spectroscopy were used for determining the number of layers, as well as to study the surface morphology and structural quality of $MoTe_2$ using a combined AFM-confocal Raman spectroscopy (AIST-NT, Horiba Jobin-Yvon Xplora)

system under ambient atmosphere. The AFM measurements were performed using an AIST-NT scanning probe microscopy system in a contact mode configuration with standard Al coated Si cantilevers with a spring constant of 40 N m^{-1} and a nominal tip radius of ≈8 nm.

Raman measurements were acquired in backscattering configuration using a Horiba confocal Raman microscope equipped with an air-cooled charge coupled device (CCD) detector. The $MoTe_2$ samples were excited with linearly polarized CW solid-state lasers of 532 or 638 nm wavelengths. The spectra were collected by an Olympus 100 × objective (0.90 N.A.) and dispersed by 2400 grooves mm^{-1} grating with slit and hole apertures set at 50 and 100 μm, respectively, providing a spectral resolution of ≈1 cm^{-1}. The laser spot size was less than 0.5 μm and only flakes larger than 1 μm were used for Raman characterization to eliminate unwanted contributions from the flake edges. In order to avoid unintentional laser-induced heating or etching of $MoTe_2$ flakes, all Raman spectra were acquired at a low humidity level of ≈30% RH and a low laser power density of ≈0.02 mW μm^{-2}, with the acquisition time set at 30 s, providing optimum signal-to-noise ratio. Raman mapping images were also acquired under these conditions by using a motorized xyz stage with a step size of 400 nm and an acquisition time of 2 s at each point. The Si first-order Raman mode at 520.7 cm^{-1} is used as reference for the $MoTe_2$ peak frequency calibration.

PL Spectroscopy: The room temperature PL measurements were performed using a Horiba Jobin-Yvon LabRam HR Raman/PL spectrometer equipped with a liquid nitrogen cooled InGaAs array detector. The spectra were collected by exciting an Ar$^+$ laser (532 nm) on to $MoTe_2$ flakes for 30 s with typical laser power density of ≈0.05 mW μm^{-2} via a 100 × objective lens (0.90 N.A.) and dispersed by 600 grooves mm^{-1} grating.

Photochemical Thinning Set-Up: Laser thinning was performed using the combined AFM-Raman system (AIST-NT, Horiba Jobin-Yvon Xplora) described above, which is enclosed in a humidity controlled environmental chamber, as shown in Figure 1a (main text). The chamber operates at a constant atmospheric pressure and temperature (≈20°C), with the ability to control the RH levels from ≈30% RH to ≈90% RH. This is done through the use of a humidifier which pumps water vapor into the chamber and the flow rate is controlled by adjusting the digital controls attached to the humidifier. Once the Raman spectra of pristine samples were obtained with an extremely low laser power and humidity of 0.02 mW μm^{-2} and ≈30% RH, respectively, the humidity was increased to 70% RH and the samples were irradiated with a slightly higher incident power of 0.2 mW μm^{-2} to undergo photochemical thinning. Here, the samples were placed on a motorized AFM stage and raster scanned by the focused laser beam via a 100 × objective (0.9 N.A.) to thin the selected regions of the sample. We have found that at high humidity levels (70% RH), an incident power of 0.2 mW μm^{-2}, a step size of 200 nm and an exposure time of 1 ms yielded reproducible layer-by-layer thinning of $MoTe_2$, regardless of the initial sample thickness.

Device Fabrication and Electrical Measurements: $MoTe_2$ FETs were fabricated by standard e-beam lithography technique using a Nanobeam e-beam system. Cr/Au (5 nm/50 nm) metal films were deposited by thermal evaporation for source–drain contacts, followed by lift-off in acetone. The highly doped (p^{++}) Si substrate and the SiO$_2$ (300 nm) layer were used as a back gate and the gate dielectric, respectively. All fabricated samples were carefully annealed in Ar/H$_2$ (90 %/10 %) atmosphere at 200 °C for 2 h to remove PMMA resist residues from the $MoTe_2$ surfaces. The electrical measurements were performed in ambient atmosphere and in vacuum (10^{-5} Torr) at room temperature using a custom-built probe station equipped with DC voltage sources, Xitron 2000, Keithley 2700 and a multimeter, Agilent 34410A.

Photoelectrical Measurements: The photoelectrical measurements were performed in a vacuum of 10^{-5} Torr using a custom-built setup (see ref. [2] for detailed description) equipped with three different lasers (473, 514, and 685 nm) that were focused through a 50 × objective lens, creating spot sizes of 1.5 μm.[8] For all photocurrent measurements the laser spot size was focused at the center of the $MoTe_2$ channel with a fixed laser power of 6 μW (3.5 μW μm^{-2}). Spatially resolved photocurrent maps were acquired by moving the xy stage in 0.5 μm increments.

Supporting Information

Supporting Information is available from the Wiley Online Library or from the author.

Conflict of Interest

The authors declare no conflict of interest.

[1] W. Choi, N. Choudhary, G. H. Han, J. Park, D. Akinwande, Y. H. Lee, *Mater. Today* **2017**, *20*, 116.

[2] N. R. Pradhan, D. Rhodes, S. Feng, Y. Xin, S. Memaran, B.-H. Moon, H. Terrones, M. Terrones, L. Balicas, *ACS Nano* **2014**, *8*, 5911.

[3] B. Chen, H. Sahin, A. Suslu, L. Ding, M. I. Bertoni, F. M. Peeters, S. Tongay, *ACS Nano* **2015**, *9*, 5326.

[4] C. Ruppert, O. B. Aslan, T. F. Heinz, *Nano Lett.* **2014**, *14*, 6231.

[5] Y.-F. Lin, Y. Xu, S.-T. Wang, S.-L. Li, M. Yamamoto, A. Aparecido-Ferreira, W. Li, H. Sun, S. Nakaharai, W.-B. Jian, K. Ueno, K. Tsukagoshi, *Adv. Mater.* **2014**, *26*, 3263.

[6] S. Larentis, B. Fallahazad, H. C. P. Movva, K. Kim, A. Rai, T. Taniguchi, K. Watanabe, S. K. Banerjee, E. Tutuc, *ACS Nano* **2017**, *11*, 4832.

[7] Y.-Q. Bie, G. Grosso, M. Heuck, M. M. Furchi, Y. Cao, J. Zheng, D. Bunandar, E. Navarro-Moratalla, L. Zhou, D. K. Efetov, T. Taniguchi, K. Watanabe, J. Kong, D. Englund, P. Jarillo-Herrero, *Nat. Nanotechnol.* **2017**, *12*, 1124.

[8] T. J. Octon, V. K. Nagareddy, S. Russo, M. F. Craciun, C. D. Wright, *Adv. Opt. Mater.* **2016**, *4*, 1750.

[9] Z. Feng, Y. Xie, J. Chen, Y. Yu, S. Zheng, R. Zhang, Q. Li, X. Chen, C. Sun, H. Zhang, W. Pang, J. Liu, D. Zhang, *2D Mater.* **2017**, *4*, 025018.

[10] J. C. Park, S. J. Yun, H. Kim, J.-H. Park, S. H. Chae, S.-J. An, J.-G. Kim, S. M. Kim, K. K. Kim, Y. H. Lee, *ACS Nano* **2015**, *9*, 6548.

[11] L. Zhou, K. Xu, A. Zubair, A. D. Liao, W. Fang, F. Ouyang, Y.-H. Lee, K. Ueno, R. Saito, T. Palacios, J. Kong, M. S. Dresselhaus, *J. Am. Chem. Soc.* **2015**, *137*, 11892.

[12] J. H. Huang, K. Y. Deng, P. S. Liu, C. T. Wu, C. T. Chou, W. H. Chang, Y. J. Lee, T. H. Hou, *Adv. Mater. Interfaces* **2017**, *4*, 1700157.

[13] T. W. Kim, H. Park, D. H. Joung, D. H. Kim, R. Lee, C. H. Shin, M. Diware, W. Chegal, S. H. Jeong, J. C. Shin, J. Park, S.-W. Kang, *Adv. Mater. Interfaces* **2018**, *5*, 1800439.

[14] A. Roy, H. C. P. Movva, B. Satpati, K. Kim, R. Dey, A. Rai, T. Pramanik, S. Guchhait, E. Tutuc, S. K. Banerjee, *ACS Appl. Mater. Interfaces* **2016**, *8*, 7396.

[15] K. K. Amara, L. Chu, R. Kumar, M. Toh, G. Eda, *APL Mater.* **2014**, *2*, 092509.

[16] X. Lu, M. I. B. Utama, J. Zhang, Y. Zhao, Q. Xiong, *Nanoscale* **2013**, *5*, 8904.

[17] Y. Liu, H. Nan, X. Wu, W. Pan, W. Wang, J. Bai, W. Zhao, L. Sun, X. Wang, Z. Ni, *ACS Nano* **2013**, *7*, 4202.

[18] A. Castellanos-Gomez, M. Barkelid, A. M. Goossens, V. E. Calado, H. S. J. van der Zant, G. A. Steele, *Nano Lett.* **2012**, *12*, 3187.

[19] S. Kim, J. H. Kim, D. Kim, G. Hwang, J. Baik, H. Yang, S. Cho, *2D Mater.* **2017**, *4*, 024004.

[20] G. H. Han, S. J. Chae, E. S. Kim, F. Güneş, I. H. Lee, S. W. Lee, S. Y. Lee, S. C. Lim, H. K. Jeong, M. S. Jeong, Y. H. Lee, *ACS Nano* **2010**, *5*, 263.

[21] L. Hu, X. Shan, Y. Wu, J. Zhao, X. Lu, *Sci. Rep.* **2017**, *7*, 15538.

[22] J. Lu, J. H. Lu, H. Liu, B. Liu, K. X. Chan, J. Lin, W. Chen, K. P. Loh, C. H. Sow, *ACS Nano* **2014**, *8*, 6334.

[23] A. Castellanos-Gomez, M. Buscema, R. Molenaar, V. Singh, L. Janssen, H. S. J. van der Zant, G. A. Steele, *2D Mater.* **2014**, *1*, 011002.

[24] H. M. Oh, G. H. Han, H. Kim, J. J. Bae, M. S. Jeong, Y. H. Lee, *ACS Nano* **2016**, *10*, 5230.

[25] B. C. T. Khac, K.-J. Jeon, S. T. Choi, Y. S. Kim, F. W. DelRio, K.-H. Chung, *ACS Appl. Mater. Interfaces* **2016**, *8*, 2974.

[26] M. Yamamoto, S.-T. Wang, M. Ni, Y.-F. Lin, S.-L. Li, S. Aikawa, W.-B. Jian, K. Ueno, K. Wakabayashi, K. Tsukagoshi, *ACS Nano* **2014**, *8*, 3895.

[27] A. Bera, D. V. S. Muthu, A. K. Sood, *J. Raman Spectrosc.* **2018**, *49*, 100.

[28] G. Froehlicher, E. Lorchat, S. Berciaud, *Phys. Rev. B* **2016**, *94*, 085429.

[29] S. Cho, S. Kim, J. H. Kim, J. Zhao, J. Seok, D. H. Keum, J. Baik, D.-H. Choe, K. J. Chang, K. Suenaga, S. W. Kim, Y. H. Lee, H. Yang, *Science* **2015**, *349*, 625.

[30] C. I. H. Ashby, *Appl. Phys. Lett.* **1998**, *46*, 752.

[31] F. A. Houle, *Phys. Rev. B* **1989**, *39*, 10120.

[32] I. Bobrinetskiy, A. Emelianov, A. Nasibulin, I. Komarov, N. Otero, P. M. Romero, *J. Phys. D: Appl. Phys.* **2016**, *49*, 41LT01.

[33] K. Wang, Y. Feng, C. Chang, J. Zhan, C. Wang, Q. Zhao, J. N. Coleman, L. Zhang, W. J. Blau, J. Wang, *Nanoscale* **2014**, *6*, 10530.

[34] A. De Sanctis, I. Amit, S. H. Nature, *Nat. Commun.* **2018**, *9*, 1652.

[35] H.-L Liu, C.-C Shen, S.-H. Su, C.-L Hsu, M.-Y. Li, L.-J. Li, *Appl. Phys. Lett.* **2014**, *105*, 201905.

[36] S. Pan, F. Ceballos, M. Z. Bellus, P. Zereshki, H. Zhao, *2D Mater.* **2017**, *4*, 015033.

[37] X. Liu, Y.-W. Zhang, *Chin. Phys. B* **2018**, *27*, 034402.

[38] A. Shafique, Y.-H. Shin, *Phys. Chem. Chem. Phys.* **2017**, *19*, 32072.

[39] N. J. Townsend, I. Amit, M. F. Craciun, S. Russo, *2D Mater.* **2018**, *5*, 025023.

[40] Y.-F. Lin, Y. Xu, C. Y. Lin, Y. W. Suen, M. Yamamoto, S. Nakaharai, K. Ueno, K. Tsukagoshi, *Adv. Mater.* **2015**, *27*, 6612.

[41] W. Luo, M. Zhu, G. Peng, X. Zheng, F. Miao, S. Bai, X. A. Zhang, S. Qin, *Adv. Func. Mater.* **2018**, *6*, 1704539.

[42] C. Kim, I. Moon, D. Lee, M. Choi, F. Ahmed, S. Nam, Y. Cho, H.-J. Shin, S. Park, W. Yoo *ACS Nano* **2017**, *11*, 1588.

[43] H. Huang, J. Wang, W. Hu, L. Liao, P. Wang, X. Wang, F. Gong, Y. Chen, G. Wu, W. Luo, H. Shen, T. Lin, J. Sun, X. Meng, X. Chen, J. Chu, *Nanotechnology* **2016**, *27*, 445201.

[44] M. Kuiri, B. Chakraborty, A. Paul, S. Das, A. K. Sood, A. Das, *Appl. Phys. Lett.* **2016**, *108*, 063506.

[45] Y. Chen, X. Wang, G. Wu, Z. Wang, H. Fang, T. Lin, S. Sun, H. Shen, W. Hu, J. Wang, J. Sun, X. Meng, J. Chu, *Small* **2018**, *14*, 1703293.

[46] A. Pezeshki, S. Hossein, H. Shokouh, T. Nazari, K. Oh, S. Im, *Adv. Mater.* **2016**, *28*, 3216.